PNAS

Supporting Information for

Microtubule detyrosination drives symmetry-breaking to polarize cells for directed cell migration

Kirstine Lavrsen, Girish Rajendraprasad, Marcin Leda, Susana Eibes, Elisa Vitiello, Vasileios Katopodis, Andrew B. Goryachev and Marin Barisic

Correspondence to: barisic@cancer.dk

This PDF file includes:

SI Materials and Methods
Figures S1 to S7
Table S1
SI References
Legends for Movies S1 to S8

Other supporting materials for this manuscript include the following:

Movies S1 to S8

Supporting Information Materials and Methods

Cell lines

The immortalized human retinal epithelial cell line hTERT RPE-1 (ATCC), hTERT RPE-1 cells stably expressing H2B-GFP (gift from H. Maiato, Institute for Research and Innovation in Health – i3S, Porto, Portugal) (1) and RPE-1 cells stably expressing Vincullin-GFP (gift from M. Balland, Laboratoire Interdisciplinaire de Physique, Grenoble Alpes University, St. Martin d'Heres, France) (2) were grown in DMEM/F12 supplemented with 10% FBS. Human osteosarcoma cell line parental U2OS or U2OS cells stably expressing EB1-GFP (gift from P. Draber, IMG ASCR, Prague, Czech Republic) (3), were grown in Dulbecco's Modified Eagle Medium (DMEM) supplemented with 10% fetal bovine serum (FBS; Invitrogen). All cell lines were cultured at 37°C in humidified conditions with 5% CO2.

RNAi, plasmids and drugs

RNAi: Cells were transfected at 30-50% confluency using Lipofectamine RNAiMAX (Thermo Fisher Scientific) with the following siRNAs for 72h:
Control siRNA 5′ UGGUUUACAUGUCGACUAA 3′ (D-001810-01-05, Dharmacon Inc.); TTL 5' GUGCACGUGAUCCAGAAAU 3′ (4); TTL-II 5' CCCUGAAUCUUAUGUGAUU 3' (4); VASH1-A 5′ CCAGACUAGGAUGCUUCUG 3′ (5); VASH2-A 5′ GGAUAACCGUAACUGAAGU 3′ (5); VASH1-B 5′ CCAGACUAGGAUGCUUCUG 3′ (5); VASH2-B 5′ CCUUAUAGUGUAAUUCAGU 3′ (5); α-TAT1 5' AACCGCCAUGUUGUUUAUAUU 3' (6); MCAK 5′ GAUCCAACGCAGUAAUGGU 3′ (7); KIF5B 5' UGAAUUGCUUAGUG UGAA 3' (8); KIF3A 5' CUAUCAGUACAUUACGGUA 3' (9); APC 5' GACGUUGCGAGAAGUUGGA 3' (10).
For knockdown of vasohibins a combination of VASH1-A and VASH2-A (siVASH) or VASH1-B and VASH2-B (siVASH-II) siRNAs were used.

Plasmids: For expression of GFP-Rab6, cells were transfected with 1–2 µg of the pEGFP-Rab6A (gift from A. Akhmanova, Department of Biology, Utrecht University, Utrecht, Netherlands) (11) construct using GeneJuice (Merck) transfection reagent according to manufacturer's protocol.

Drugs: Microtubule stabilization or destabilization during single cell migration was attained by addition of 10 nM Taxol (Paclitaxel, LC laboratories) or 3 µM Nocodazole (Sigma-Aldrich) to the culture medium before starting of imaging.

Cell migration in 1D

Linear micropatterns (CYTOOchips™ Motility A ×18, CYTOO) were coated with 0.02 mg/ml fibronectin (Sigma-Aldrich F4759) for 30min before washing with PBS twice and assembled onto a 4-well chamber (CYTOO). Cells were seeded onto each quadrant of the micropatterns and allowed to adhere for two hours. Bright-field time-lapse imaging was performed in a heated incubation chamber (37 °C) with controlled humidity and CO_2 supply (5%), using EC Plan-Neofluar 10x/0.3NA objective mounted on an inverted Zeiss Axio Observer Z1 microscope (Marianas Imaging Workstation from Intelligent Imaging and Innovations Inc. (3i), Denver, CO, USA) and images were captured every 10 min using ORCA-Flash 4.0 digital CMOS camera (Hamamatsu).

The kymograph trajectories were obtained by manual tracking of cell front and rear on lines on 5 µm width using custom MATLAB script (2). Cell migration was quantified by tracking the cell centroid during six hours and the cell length was measured from the last time-frame using ImageJ (National Institute of Health, Bethesda, MD, USA). Number of contractile events characterized by retraction of the rear were quantified manually.

Immunoblots and immunofluorescence microscopy

Immunoblots were performed as described before (12). For anti-APC immunoblots, cells were lysed directly by addition of Laemmli sample buffer (Biorad) and the proteins were separated on SDS-PAGE followed by transfer onto nitrocellulose membrane. The following primary antibodies were used in this study: mouse anti-α-tubulin (1:2000; Sigma-Aldrich T5168, B-5-1-2), rabbit anti-detyrosinated α-tubulin (1:20000; home-made) (5), mouse anti-acetylated α-tubulin (1:500; Sigma-Aldrich MABT868, 6-11B-1), mouse anti-MCAK (1:1000; Abnova

H00011004-M01), rabbit anti-KIF5B (1:2000; Abcam ab167429, EPR10276(B)), rabbit anti-KIF3A (1:2000; Abcam ab11259), mouse anti-APC (1:1000; Santa Cruz Biotechnology sc-53165), rabbit anti-TTL (1:1000; Proteintech 13618-1-AP), mouse anti-GAPDH (1:25000; Proteintech 60004-1-Ig), mouse anti-Vinculin (1:5000; Sigma-Aldrich SAB4200729, Vin-11-5), HRP-conjugated secondary antibodies (1:10000; Jackson ImmunoResearch), and visualized using ECL system (Bio-Rad) or SuperSignal™ (Thermo Fisher Scientific).

Cells were seeded onto fibronectin coated micropatterns (CYTOOchips™ Motility A×18, CYTOO 10-031-00-18) and allowed to adhere overnight at 37°C with 5% CO2. Cells were fixed using ice-cold methanol for 3 min at -20°C or 4% paraformaldehyde in PHEM buffer for 20 min at 37°C as described before (13). Following wash with phosphate-buffered saline (PBS), cells were immunostained with target specific primary and Alexa Fluor-conjugated secondary antibodies (1:1000; Thermo Fisher Scientific) diluted in IF stain (1x PBS, 1% FBS, 0.5% Tween). DNA was counterstained with DAPI (final concentration 0.1 µg/ml, Sigma-Aldrich D9542) and mounted on glass slides using Fluoromount-G mounting media (Southern Biotech 0100-01). The primary antibodies used for staining were mouse anti α-tubulin (1:1000; Sigma-Aldrich T5168, B-5-1-2), rabbit anti-detyrosinated α-tubulin (1:1000; home-made) (5), rabbit anti-APC (1:100; gift from I. Nathke, School of Life Sciences, University of Dundee, Dundee) (14), mouse anti-acetylated α-tubulin (1:50; Sigma-Aldrich MABT868, 6-11B-1), rabbit anti-myosin IIB (1:1000; BioLegend 909901) and mouse anti-Rac1 (1:100; BD biosciences 610650, clone 102/Rac1 (RUO)). Phalloidin-iFluor 555 (1:1000, Abcam ab176756) was used to visualize actin. Images were acquired using LSM700 or LSM800 confocal microscope (Carl Zeiss Microimaging Inc.) mounted on a Zeiss Axio imager Z1 equipped with plan-apochromat 63×/1.40 oil DIC M27 objective (Carl Zeiss, Inc.) and Zen software (Carl Zeiss, Inc.).

For analysis of polarity, cells were divided into two parts by a line through the center of the nucleus perpendicular to the 1D migration on micropatterns. The polarity was calculated from sum-projected images as the integrated density in one part of the cell divided by the integrated density in the other part of the cell. The data is presented as absolute values in a Log_2 scale (log_2(side1/side2)).

For quantification of distribution of proteins across cells on micropatterns, line scan function from ImageJ was used. The cells were divided into 1 µm segments perpendicular to the axis of migration and mean grey values were extracted from the sum-projected images. For quantification of intensities independent of cell size, the length of the cells was normalized and presented as percentage of total cell length. In case of quantification of detyrosinated tubulin distribution, line scan was performed from the edge of the nucleus to the leading edge. Polarity at cell periphery was quantified as the ratio of intensities in 10% of normalized area of the edges of the two sides (marked a,b in figures).

The detyrosinated tubulin levels were quantified from integrated densities of individual cells from sum-projections of images along the z-plane and normalized to the total α-tubulin levels.

Analysis of focal adhesion dynamics

For analysis of focal adhesion dynamics, RPE-1 cells stably expressing Vincullin-GFP were seeded on fibronectin coated micropatterns and allowed to adhere overnight. Dynamics of Vincullin-GFP were imaged every 1 min for 3 hours in a heated incubation chamber (37 °C) with controlled humidity and CO_2 supply (5%), using a Plan-Apochromat DIC 63×/1.4NA oil objective mounted on an inverted Zeiss Axio Observer Z1 microscope, equipped with a CSU-X1 spinning-disk confocal head (Yokogawa Corporation of America) and four laser lines (405 nm, 488 nm, 561 nm and 640 nm). Images were detected using an iXon Ultra 888 EM-CCD camera (Andor Technology).

Focal adhesion turnover analysis was performed only from focal adhesions that underwent the complete assembly and disassembly cycle. Fluorescence intensities of two to three random focal adhesions from each side were tracked manually using ImageJ. A region of interest (ROI) was drawn around the focal adhesion and mean fluorescence intensity was measured. The size and position of ROI was adjusted during the time-lapse series to obtain accurate intensity measurements. The assembly and disassembly rate constants were obtained from three-frame running averaged normalized fluorescence intensity curve. The assembly and disassembly phases of the curve were fit to logistic and single exponential decay functions to obtain the rate

constants in GraphPad Prism (15). The focal adhesion lifetimes were quantified by counting the number of sequential frames from assembly through disassembly. Number of focal adhesions were quantified by setting threshold and analyze particle function in ImageJ followed by normalization to the cell area.

EB1 and Rab6 tracking

U2OS EB1-GFP cells or RPE-1 cells transiently transfected with GFP-Rab6 were cultured on fibronectin coated micropatterns. Spinning-disk confocal time-lapse images were collected every 0.5 second. About 5 to 12 EB1-GFP comets or GFP-Rab6 vesicles per cell were tracked manually to obtain distance, lifespan and velocity parameters using ImageJ as described before (16). Cells grown on lines were divided into two parts as described earlier, to be able to compare the polarity of different parameters.

Gap closing assay

RPE-1 or RPE-1 cells stably expressing H2B-GFP cells treated with control or target specific siRNAs for 48h were seeded in Ibidi Culture-Insert 2-Well µ-Plate wells. After incubating at 37 °C overnight, cell culture inserts were carefully removed. Gap closing was monitored by live cell imaging where images were taken at 1h time interval using EC Plan-Neofluar 10x/0.3NA objective mounted on an inverted Zeiss Axio Observer Z1 microscope using ORCA-Flash 4.0 digital CMOS camera (Hamamatsu). The void gap area was measured using ImageJ manually and normalized to starting time-point to obtain the percentage of gap closure. Number of cells in the gap area were quantified by manual counting of the nucleus marked by H2B-GFP signal.

For analysis of detyrosinated/total α-tubulin distribution, cells were fixed using ice-cold methanol and immunostained as described above at indicated time intervals and imaged using LSM700 confocal microscope.

3D migration assay and analysis

For analysis of RPE-1 cell migration in 3D matrix, about 2500 cells in 50µl was mixed with 50µl of Matrigel (Corning) to achieve a final concentration of 4.8 mg/ml and incubated at 37 °C for 2 hours to allow gelling of the matrix. Following incubation, phase-contrast imaging was performed using EC Plan-Neofluar 10x/0.3NA objective mounted on an inverted Zeiss Axio Observer Z1 microscope using ORCA-Flash 4.0 digital CMOS camera (Hamamatsu) at 15 min intervals.

The number of protrusions and protrusion angle between the longest protrusion and other protrusions were quantified manually using ImageJ. The polar distribution plots were obtained using a custom MATLAB script.

Manual tracking of individual cell migration was performed using ImageJ to obtain the velocity and coordinates of cell tracks. Subsequently, the trajectory flower plots and MSD analysis were performed using the open-source algorithm, DiPer (17).

Statistical analysis

All graphs and statistical analysis were generated in GraphPad Prism 8.0. Data points were tested for normality using D'Agostino & Pearson test. Accordingly, statistical significance was determined by Student's *t*-test (unpaired, two-tailed; normal distribution) or Mann-Whitney *U*-test (unpaired, two-tailed; no normal distribution). F-test was used to compare variances and Welch's correction was employed when variances were not equal. For multiple comparisons (Figs. 2E, 3B-C, S2E-F and S3H), one-way ANOVA was used. Details of the statistical significance and n values for each conditions can be found in the figures and figure legends.

Model construction and analysis

Cells spread on the 1D adhesive support (**Figs. 1,2**) have highly elongated shapes with a characteristic length $L \approx 100\,\mu m$ and width $\Delta \approx 5\,\mu m$. Thus, their geometric aspect ratio $\Delta/L \approx 0.05$ is so small that we can model them as 1D objects with length L. Analysis of fluorescence images of MTs in these cells shows that they form two highly polarized bundles emanating from the centrosome positioned underneath the nucleus in the middle of the cell (**Fig. 3A**). Furthermore, fluorescence microscopy movies of EB1 comets reveal that, unless

MTs encounter the cell side edge at a nearly right angle, MT plus ends slip along the membrane while the MTs continue to extend towards the left and right cell ends, a well-known behavior which was observed experimentally (18) and studied theoretically (19). Therefore, we approximate the cellular microtubule array by right and left bundles of equal length with their minus ends anchored at the centrosome $x = \pm 0$ and their plus ends reaching the respective cell ends at $x = \pm L/2$ (**Fig. S4H**). To simplify the model analysis, we neglect augmin-mediated MT nucleation and assume that all MTs have equal length $L/2$. The two bundles are then quantitatively characterized by their time-dependent densities, $\rho_R(t)$ and $\rho_L(t)$.

The APC-kinesin-1 complex (further, APC) is represented by its free cytoplasmic concentration $c(x,t)$ and microtubule-bound density $m(x,t)$. APC binds to MTs with the rate k_{on}, dissociates from them with the rate k_{off} and diffuses in the cytoplasm with the diffusion coefficient D. To account for the documented APC complex-formation at least in part, we assumed that the cytoplasmic diffusion coefficient of APC is a free parameter, allowed to vary from values appropriate for APC monomers to those of large oligomers. The microtubule-bound fraction of APC advectively migrates to the plus ends with the constant velocity $\pm v$. This assumption also requires that APC that arrives at the plus ends "walks off" the MTs without a delay and, thus, no traffic jams form anywhere along the MTs (20). With these assumptions and notations, the model takes the form:

$$\begin{cases} \dot{m} = \pm v \frac{\partial m}{\partial x} + k_{on}\rho_{R,L}c - k_{off}m \\ \dot{c} = D\frac{\partial^2 c}{\partial^2 x} - k_{on}\rho_{R,L}c + k_{off}m \end{cases}, \quad [1]$$

where the dependence of variables on x and t is omitted for brevity and the values of parameters are given in Table S1. Boundary conditions at the cell ends are obtained by integrating the mass conservation relationship

$$\left(\pm vm + D\frac{\partial c}{\partial x}\right)\Big|_{x=\pm L/2} = 0. \quad [2]$$

At the steady state, when the net exchange of APC between right and left sides of the cell ceases, $\partial c(0)/\partial x = 0$.

Dynamics of the model [1-2] is described by a hierarchy of characteristic times, of which the reaction time, which is required to establish a local binding equilibrium of APC between the cytoplasm and MTs, $\tau_r = 1/(k_{on} + k_{off}) < 1$ sec is the shortest. Advection time $\tau_a = L/v = 250$ sec defines an intermediate time scale. Since the velocity of polymerizing and depolymerizing MT plus ends is of the same order as a typical velocity of kinesin motors (21, 22), we may assume that the characteristic time τ_m, on which MT polymerization dynamics equilibrates with the change in the spatial distribution of signaling molecules within the cell, is comparable to the advection time: $\tau_m \approx \tau_a$. On the other hand, the diffusion time $\tau_d = L^2/D = 10^3 - 10^4$ sec (assuming $D = 10 - 1\,\mu m^2/sec$) determines the time scale on which the entire model [1-2] reaches its steady state and is by far the longest in the system $\tau_d > \tau_a \approx \tau_m \gg \tau_r$. Thus, on the time scale $\tau \approx \tau_d$ of model [1-2] reaching its steady state we can coarse-grain the detailed polymerization-depolymerization dynamics of individual MTs and assume that the densities of polymerized MTs in left and right bundles are produced and depolymerized with constant rates k_1 and, k_{-1}, respectively. In the absence of the APC-dependent positive feedback, the densities of MT bundles are constant in time and $\rho_R(t) = \rho_L(t) = \rho_S$. In this simple case, model [1-2] at all parameter values has a unique stable solution that describes the symmetric distribution of APC both on the microtubules and in the cytoplasm (**Fig. 6D**, green curve).

To introduce the APC-dependent positive feedback into model [1-2], we further assume that the MT bundles are disassembled with the rate dependent on the cytoplasmic concentration of APC at the bundle ends, $C_{APC}(R) \equiv c(L/2,t)$ and $C_{APC}(L) \equiv c(-L/2,t)$. Then the temporal dynamics of the coarse-grained MT density on either side of the cell can be described by a chemical kinetic equation:

$$\dot{\rho}_{R,L} = k_1 - \rho_{R,L}\left(k_{-1}^0 + \frac{k_{-1}^1}{1+\delta_{R,L}/\delta'}\right), \quad [3]$$

where $\delta_{R,L}$ is a shortened notation for $C_{APC}(R)$ and $C_{APC}(L)$ and the unknown values of MT dynamic parameters, the rate of MT formation k_1, the rate of MT constitutive disassembly k_{-1}^0, the rate of MT APC-inhibited disassembly k_{-1}^1, and the characteristic APC concentration δ' are defined below. In formulating [3] we assumed that the characteristic rate of MT disassembly is determined largely by the frequency of MT catastrophe (kinetic bottleneck), as the rate of MT depolymerization, as such, is very high *in vivo* (23). Thus, once the MT disassembly is initiated

at its plus end at the APC-dependent catastrophe rate, the following depolymerization can be considered as essentially instantaneous on the time scale $\tau \approx \tau_d$. Therefore, the rate of APC-inhibited MT disassembly in [3] is determined by $\delta_{R,L}$, the cytoplasmic concentration of APC at the MT plus ends, where a catastrophe event initiates MT disassembly.

Leveraging separation of the characteristic times $\tau_d > \tau_m$, we can apply quasi-steady-state approximation to [3] and express $\rho_{R,L}$ as an explicit function of $\delta_{R,L}$:

$$\rho_{R,L} = k_1 \left(k_{-1}^0 + \frac{k_{-1}^1 \delta'}{\delta' + \delta_{R,L}} \right)^{-1}. \quad [4]$$

At the saturating bundle-end concentrations of APC (*i.,e.*, when $\delta_{R,L} \to \infty$), the lifetime of the MTs in the bundle reaches its maximum value $\tau_\infty = 1/k_{-1}^0$ and so does the MT density $\rho_\infty = k_1/k_{-1}^0$. In contrast, at $\delta_{R,L} = 0$ the MT lifetime is the shortest $\tau_0 = 1/(k_{-1}^0 + k_{-1}^1)$ and the MT density is the lowest $\rho_0 = k_1/(k_{-1}^0 + k_{-1}^1)$. In the Results, we defined the strength of the APC-dependent positive feedback as the ratio of the characteristic MT lifetimes $\chi = \tau_\infty/\tau_0$. In the notations introduced above

$$\chi = \frac{\tau_\infty}{\tau_0} = \frac{\rho_\infty}{\rho_0} = 1 + \frac{k_{-1}^1}{k_{-1}^0}. \quad [5]$$

Now we can express the unknown values k_1, k_{-1}^0 , k_{-1}^1 and δ' via χ and the parameters of the symmetric APC distribution in the absence of the APC-mediated positive feedback, *i.e.,* $\rho_{R,L} = \rho_S$ and $\delta_{R,L} = \delta_S$. If we postulate that $\rho_S = (\rho_0 + \rho_\infty)/2$, then in the so chosen parametrization

$$\rho_\infty = \frac{2\chi\rho_S}{1+\chi}\ ,\ \rho_0 = \frac{2\rho_S}{1+\chi}\ ,\ \delta' = \frac{\delta_S}{\chi}. \quad [6]$$

Using these parameters, we can now transform [4] into the expression for the non-dimensional normalized variables $\tilde{\rho} = \rho/\rho_S$ and $\tilde{\delta} = \delta/\delta_S$ as follows:

$$\tilde{\rho}_{R,L} = \frac{2(1+\chi\tilde{\delta}_{R,L})}{(1+\chi)(1+\tilde{\delta}_{R,L})}, \quad [7]$$

which can now be substituted into the model [1-2] to augment it with the APC-dependent positive feedback loop.

To model the effect of detyrosination, we adopted the following assumptions. In the Results we hypothesized that, like the lifetime of MTs itself, the binding rate of APC to detyrosinated MTs also increases monotonously with the cytoplasmic concentration of APC at the cell ends. To simplify the analysis and avoid introduction of additional unknown parameters, we further postulate that this increase is linear in a wide range of non-saturating APC concentrations and modify the APC microtubule binding rate as

$$k_{on} = k_{on}^0\left(1 + \alpha\tilde{\delta}\right), \quad [8]$$

where α is the introduced in the Results unknown strength of the effect of detyrosination on the APC microtubule transport.

Model [1] with boundary conditions [2] end extensions [7] and [8] was integrated numerically with the finite difference method using a custom C code. To initialize the simulations, we postulated that at $t = 0$ the entire cellular APC is in the cytoplasm at an arbitrarily chosen spatially uniform concentration (10 μM). Since in the vicinity of the pitchfork bifurcation symmetry breaking occurs very slowly, to expedite it in simulations, we additionally modified these initial conditions with spatially localized small-amplitude perturbations. Linear stability analysis of the model was performed numerically following the discretization of the symmetric concentration profile on a uniform grid with $N = 120$ spatial nodes and concomitant transformation into a system of $2N$ ordinary differential equations as described in detail in (24).

To produce the data plotted on **Fig. S4I**, the maximal eigenvalue λ_{max} of the unstable symmetric APC state and polarization magnitude σ were numerically computed on a rectangular grid of log-transformed non-dimensional model parameters $K_a = k_{on}^0/k_{off}$ and $d = \frac{D}{D_0}$, where $D_0 = 1\ \mu m^2/sec$, is an arbitrary constant chosen for the nondimensionalisation of the APC diffusion coefficient d. Since the time of polarity establishment in the model can be approximated as $\tau_{pol} \approx 1/\lambda_{max}$, the cell polarization efficiency $E_{pol} = \sigma/\tau_{pol}$ was computed as $E_{pol} = \sigma\lambda_{max}$. The data presented in the **Fig. 6H** was computed by pixel-wise multiplication of the data presented in **Fig. S4I** (top row) and **S4I** (bottom row), respectively.

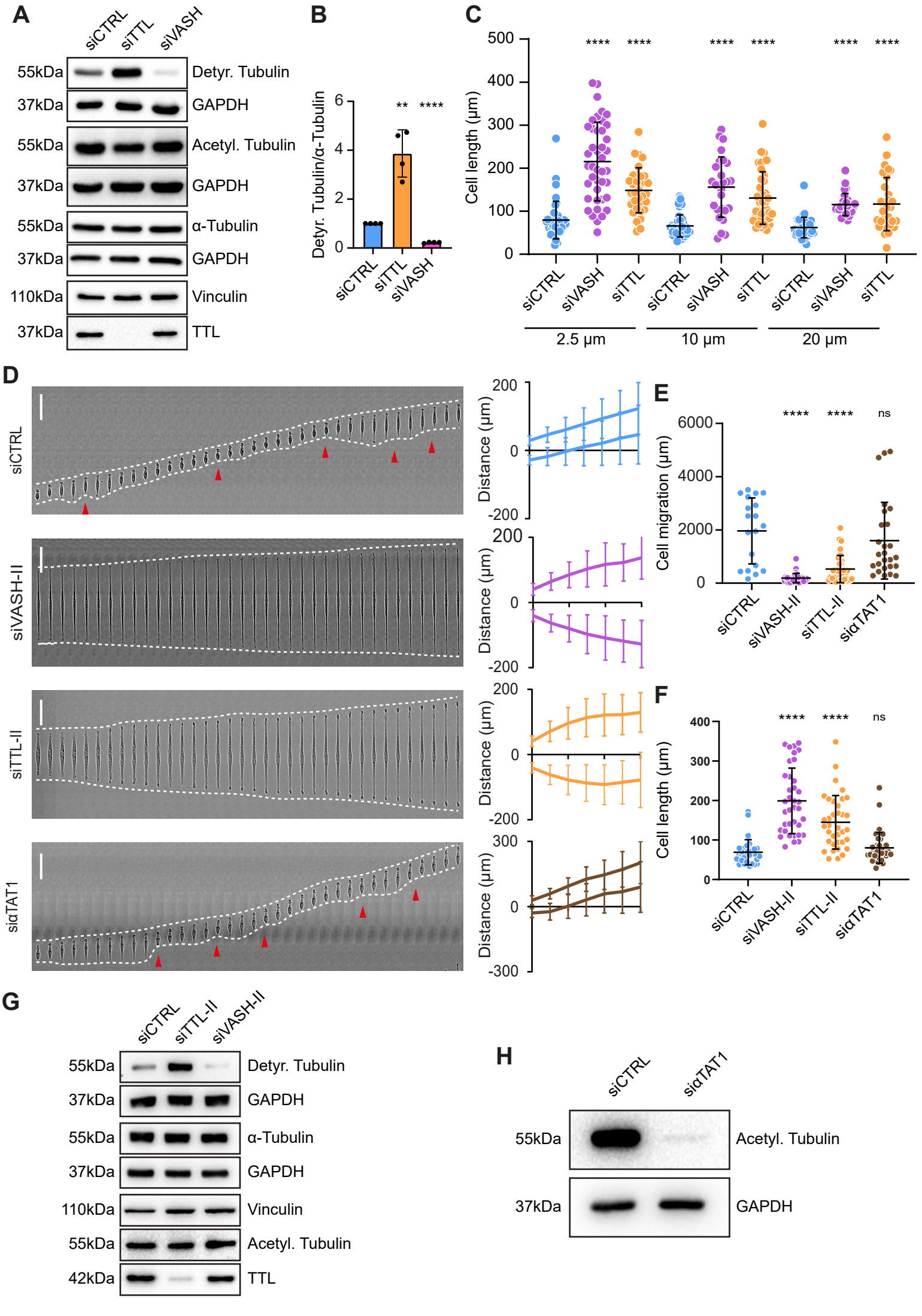
A
siCTRL
siTTL
siVASH
55kDa
Detyr. Tubulin
37kDa
GAPDH
55kDa
Acetyl. Tubulin
37kDa
GAPDH
55kDa
α-Tubulin
37kDa
GAPDH
110kDa
Vinculin
37kDa
TTL
B
Detyr. Tubulin/α-Tubulin
**
****
siCTRL
siTTL
siVASH
C
Cell length (μm)
****
siCTRL
siVASH
siTTL
2.5 μm
10 μm
20 μm
D
siCTRL
siVASH-II
siTTL-II
siαTAT1
Distance (μm)
E
Cell migration (μm)
ns
siCTRL
siVASH-II
siTTL-II
siαTAT1
F
Cell length (μm)
ns
G
siCTRL
siTTL-II
siVASH-II
55kDa
Detyr. Tubulin
37kDa
GAPDH
55kDa
α-Tubulin
37kDa
GAPDH
110kDa
Vinculin
55kDa
Acetyl. Tubulin
42kDa
TTL
H
siCTRL
siαTAT1
55kDa
Acetyl. Tubulin
37kDa
GAPDH

Fig. S1. Microtubule detyrosination is essential for cell polarity and directed cell migration

(A) Immunoblot analysis of detyrosinated and acetylated α-tubulin, total α-tubulin and tubulin tyrosine ligase (TTL) levels after RNAi mediated knockdown of VASH1 and VASH2 or TTL from RPE-1 cell lysates. GAPDH and vinculin were used as loading control.

(B) Quantification of normalized detyrosinated α-tubulin levels from 4 independent immunoblots. The bar graph shows mean ± SD.

(C) Scatter plot of cell length of RPE-1 cells with indicated treatments after 6 hours on linear micropatterns of different widths. (N, n): 2.5μm - siCTRL (40,3), siVASH (42,3), siTTL (33,3); 10μm - siCTRL (46,3), siVASH (27,3), siTTL (39,3); 20μm - siCTRL (38,3), siVASH (27,3), siTTL (30,3).

(D) Representative kymograph of RPE-1 cell migration on 5 μm linear micropatterns following treatments with control, alternative siRNAs targeting VASH1/2 and TTL and αTAT1. White dotted lines follow the edges of the cell and red arrow heads mark retraction events at the cell rear. The combined kymograph trajectories with mean ± SD are shown on the right. Scale bar, 50 μm. (N, n): siCTRL (133,18), siVASH-II (27,3), siTTL-II (36,3), siα-TAT1 (22,3).

(E, F) Scatter plot of total cell migration distance (D) and cell length (E) of RPE-1 cells treated with alternative siRNAs after 6 hours on 5 μm linear micropatterns. (N, n): Cell migration - siCTRL (19,3), siVASH-II (33,3), siTTL-II (33,3), siα-TAT1 (26,3); Cell length - siCTRL (31,3), siVASH-II (37,3), siTTL-II (36,3), siα-TAT1 (38,4).

(G) Representative immunoblots of detyrosinated and acetylated α-tubulin, total α-tubulin and TTL levels following RNAi mediated knockdown of VASH1 and VASH2 or TTL using alternative siRNAs from RPE-1 cell lysates with GAPDH and vinculin as loading control.

(H) Immunoblot from RPE-1 cell lysates treated siα-TAT1 showing acetylated α-tubulin levels and GAPDH as loading control.

N - number of cells, n - number of independent experiments. The scatter plots include mean ± SD. ns - not significant, $^{**}P \leq 0.01$, $^{****}P \leq 0.0001$.

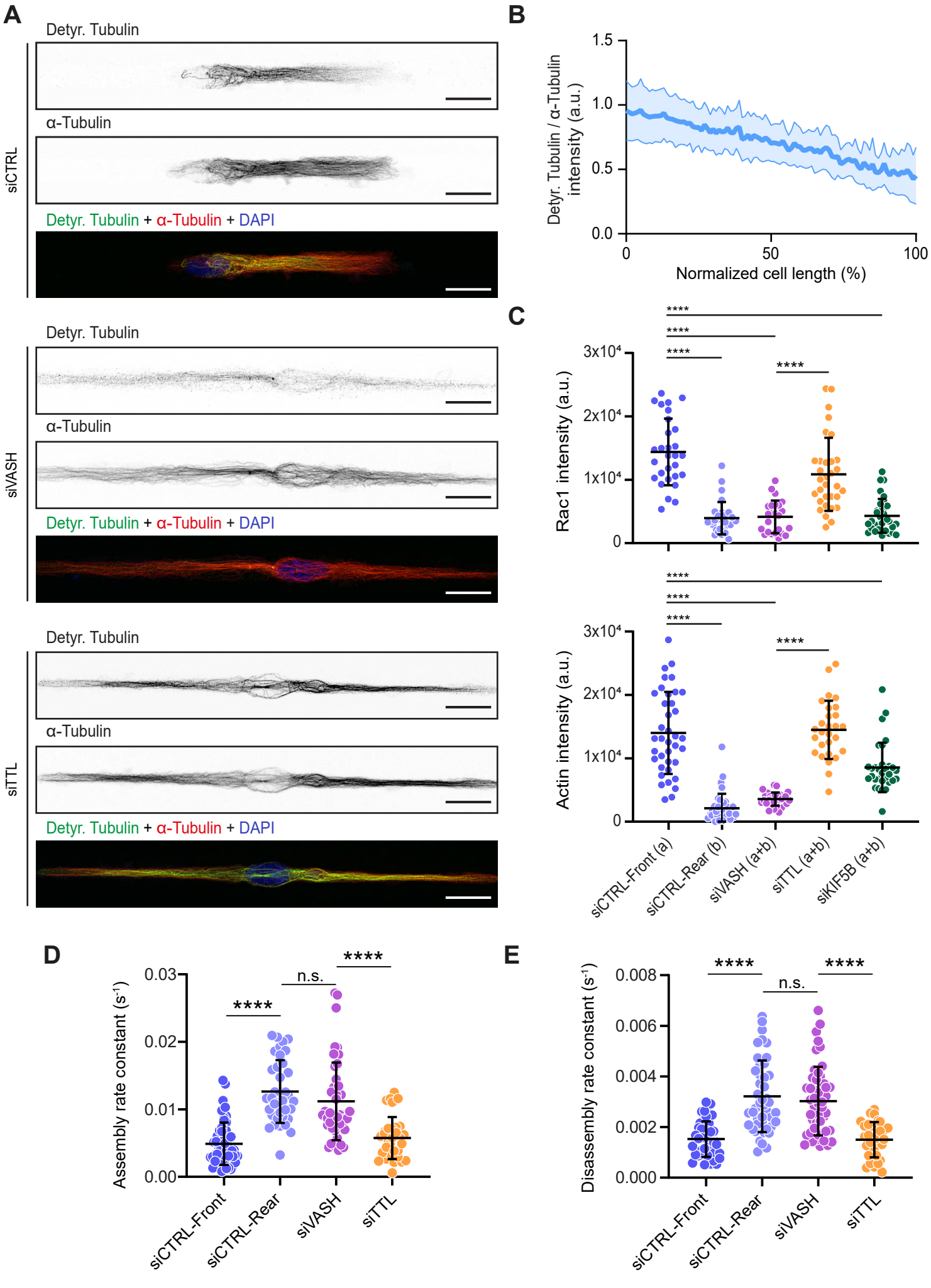
A
Detyr. Tubulin
α-Tubulin
siCTRL
Detyr. Tubulin + α-Tubulin + DAPI
Detyr. Tubulin
α-Tubulin
siVASH
Detyr. Tubulin + α-Tubulin + DAPI
Detyr. Tubulin
α-Tubulin
siTTL
Detyr. Tubulin + α-Tubulin + DAPI
B
Detyr. Tubulin / α-Tubulin intensity (a.u.)
1.5
1.0
0.5
0.0
0
50
100
Normalized cell length (%)
C
Rac1 intensity (a.u.)
3x10⁴
2x10⁴
1x10⁴
0
****
****
****
****
Actin intensity (a.u.)
3x10⁴
2x10⁴
1x10⁴
0
****
****
****
****
siCTRL-Front (a)
siCTRL-Rear (b)
siVASH (a+b)
siTTL (a+b)
siKIF5B (a+b)
D
Assembly rate constant (s⁻¹)
0.03
0.02
0.01
0.00
****
n.s.
****
siCTRL-Front
siCTRL-Rear
siVASH
siTTL
E
Disassembly rate constant (s⁻¹)
0.008
0.006
0.004
0.002
0.000
****
n.s.
****
siCTRL-Front
siCTRL-Rear
siVASH
siTTL

Fig. S2. Microtubule detyrosination is essential for cell polarity, focal adhesion dynamics and directed cell migration

(A) Representative point-scanning confocal maximum-intensity projected images of RPE-1 cells treated with indicated siRNAs on linear micropatterns immunostained for detyrosinated (Detyr. Tubulin) and total α-tubulin with DAPI as a DNA counterstain. Scale bar, 20 μm.

(B) Mean intensity profile of detyrosinated tubulin normalized to total α-tubulin obtained using line scans from nucleus till cell edge in siCTRL cell front sides. Thick line at the center represents mean and the shaded area represent SD. (N, n): (14,2).

(C) Mean Rac1 (C) and Actin (D) intensities in RPE-1 cells treated with indicated siRNAs. Data represents the sum of intensities from 10% of normalized area of the edges of the two sides (a + b). (N, n): Rac1 intensity - siCTRL (29,3), siVASH (24,3), siTTL (32,3); Actin intensity - siCTRL (38,4), siVASH (28,4), siTTL (31,4).

(D, E) Analysis of focal adhesion assembly (E) and disassembly (F) rate constants following indicated siRNA treatments. Each data point represents values of individual focal adhesions from four independent experiments. (N, n): Assembly rate - siCTRL (51,14), siVASH (49,16), siTTL (32,14); Disassembly rate - siCTRL (44,13), siVASH (49,16), siTTL (32,16).

N - number of cells, n - number of independent experiments. The scatter plots include mean ± SD. ns - not significant, ****$P \leq 0.0001$.

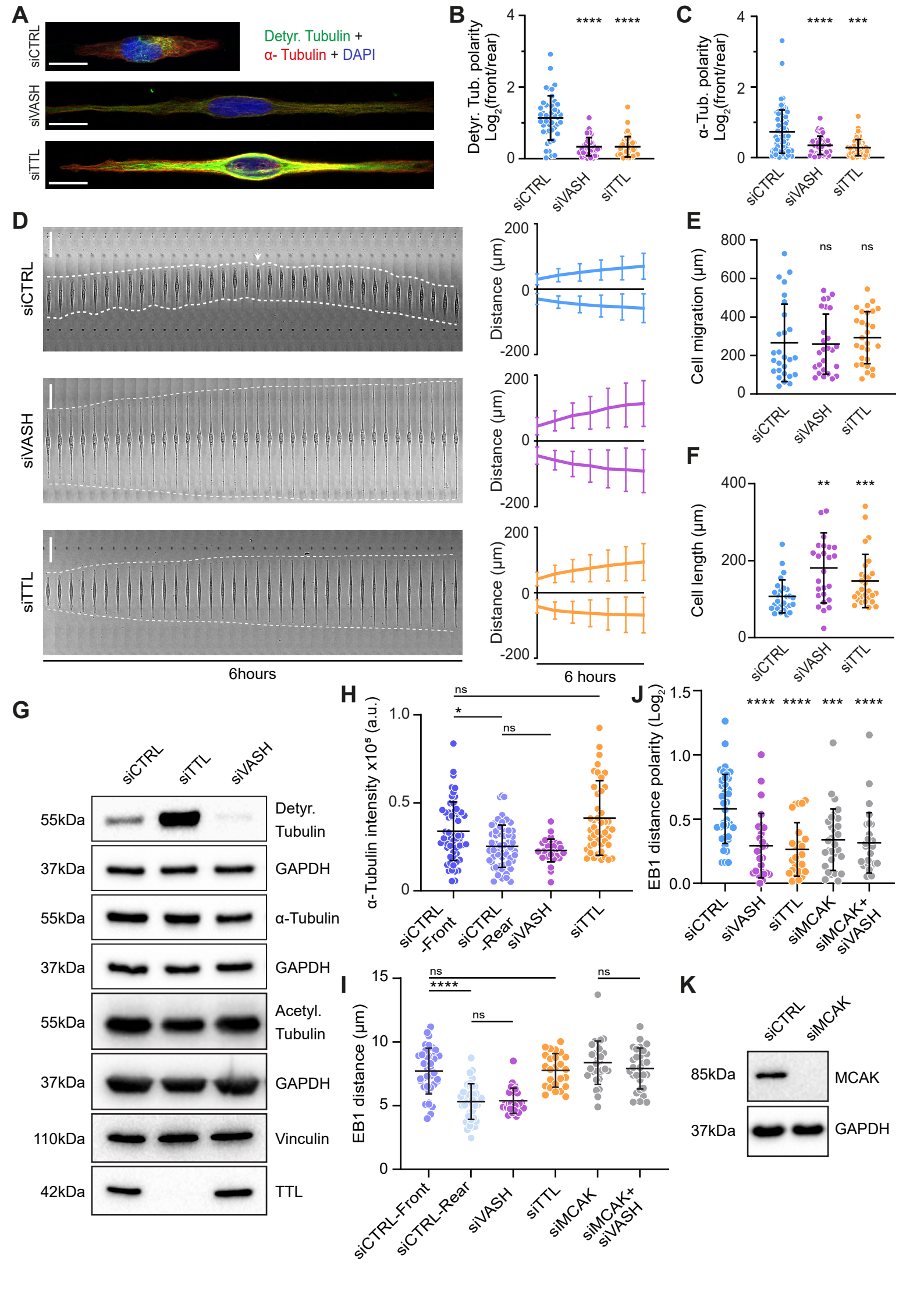
A
siCTRL
siVASH
siTTL
Detyr. Tubulin +
α- Tubulin + DAPI
B
Detyr. Tub. polarity
Log2(front/rear)
****
****
siCTRL
siVASH
siTTL
C
α-Tub. polarity
Log2(front/rear)
****
***
siCTRL
siVASH
siTTL
D
siCTRL
siVASH
siTTL
6hours
Distance (µm)
200
0
-200
6 hours
E
Cell migration (µm)
800
600
400
200
0
ns
ns
siCTRL
siVASH
siTTL
F
Cell length (µm)
400
200
0
**
***
siCTRL
siVASH
siTTL
G
siCTRL
siTTL
siVASH
55kDa
Detyr. Tubulin
37kDa
GAPDH
55kDa
α-Tubulin
37kDa
GAPDH
55kDa
Acetyl. Tubulin
37kDa
GAPDH
110kDa
Vinculin
42kDa
TTL
H
α-Tubulin intensity x10⁵ (a.u.)
1.0
0.5
0
ns
*
ns
siCTRL -Front
siCTRL -Rear
siVASH
siTTL
J
EB1 distance polarity (Log2)
1.5
1.0
0.5
0.0
****
****
***
****
siCTRL
siVASH
siTTL
siMCAK
siMCAK+ siVASH
I
EB1 distance (µm)
15
10
5
0
ns
****
ns
ns
siCTRL-Front
siCTRL-Rear
siVASH
siTTL
siMCAK
siMCAK+ siVASH
K
siCTRL
siMCAK
85kDa
MCAK
37kDa
GAPDH

Fig. S3. Microtubule detyrosination regulates microtubule dynamics during directed cell migration

(A) Representative point-scanning confocal maximum-intensity projected images of U2OS cells on linear micropatterns subject to indicated treatments immunostained with antibodies against detyrosinated (Detyr. Tubulin) and total α-tubulin with DAPI as a DNA counterstain. Scale bar, 20 μm.

(B, C) Quantification of the detyrosinated (B) and total α-tubulin (C) polarity from immunostained U2OS cells on linear micropatterns. (N, n): Detyr. Tubulin polarity - siCTRL (45,3), siVASH (42,3), siTTL (44,3); Total tubulin polarity - siCTRL (74,4), siVASH (50,4), siTTL (60,4).

(D) Representative kymograph of U2OS cell migration on 5 μm linear micropatterns following treatments with control and target specific siRNAs. White dotted lines follow the edges of the cell and white arrows indicate change in migration direction. The combined kymograph trajectories with mean ± SD are shown on the right. Scale bar, 50 μm. (N, n): siCTRL (72,3), siVASH (63,3), siTTL (67,3).

(E, F) Scatter plot of total cell migration distance (E) and cell length (F) of U2OS cells with indicated treatments after 6 hours on 5 μm linear micropatterns. (N, n): Cell migration - siCTRL (27,3), siVASH (26,3), siTTL (28,3); Cell length - siCTRL (27,3), siVASH (26,3), siTTL (28,3).

(G) Immunoblot analysis of detyrosinated, acetylated and total α-tubulin, and TTL levels after RNAi mediated knockdown of VASH1 and VASH2 or TTL from U2OS cell lysates. GAPDH and vinculin were used as loading control.

(H) Scatter plot of mean α-tubulin intensity in U2OS cells on linear micropatterns following indicated treatments. (N, n): siCTRL (57,4), siVASH (30,3), siTTL (47,3).

(I) Quantification of microtubule length (distance travelled) by manual tracking from U2OS EB1-GFP cells on linear micropatterns. (N, n): siCTRL (38,4), siVASH (25,3), siTTL (25,3), siMCAK (29,3), siMCAK + siVASH (28,3).

(J) Polarity of distance EB1-GFP comet velocity in U2OS EB1-GFP cells on linear micropatterns subjected to indicated siRNA treatments.
(K) Immunoblot analysis of lysates from U2OS cells treated with control or siMCAK siRNAs with anti-MCAK antibody used to validate siRNA mediated knockdown and GAPDH as the loading control.

N - number of cells, n - number of independent experiments. The scatter plots include mean ± SD. ns - not significant, $^{**}P \leq 0.01$, $^{***}P \leq 0.001$, $^{****}P \leq 0.0001$.

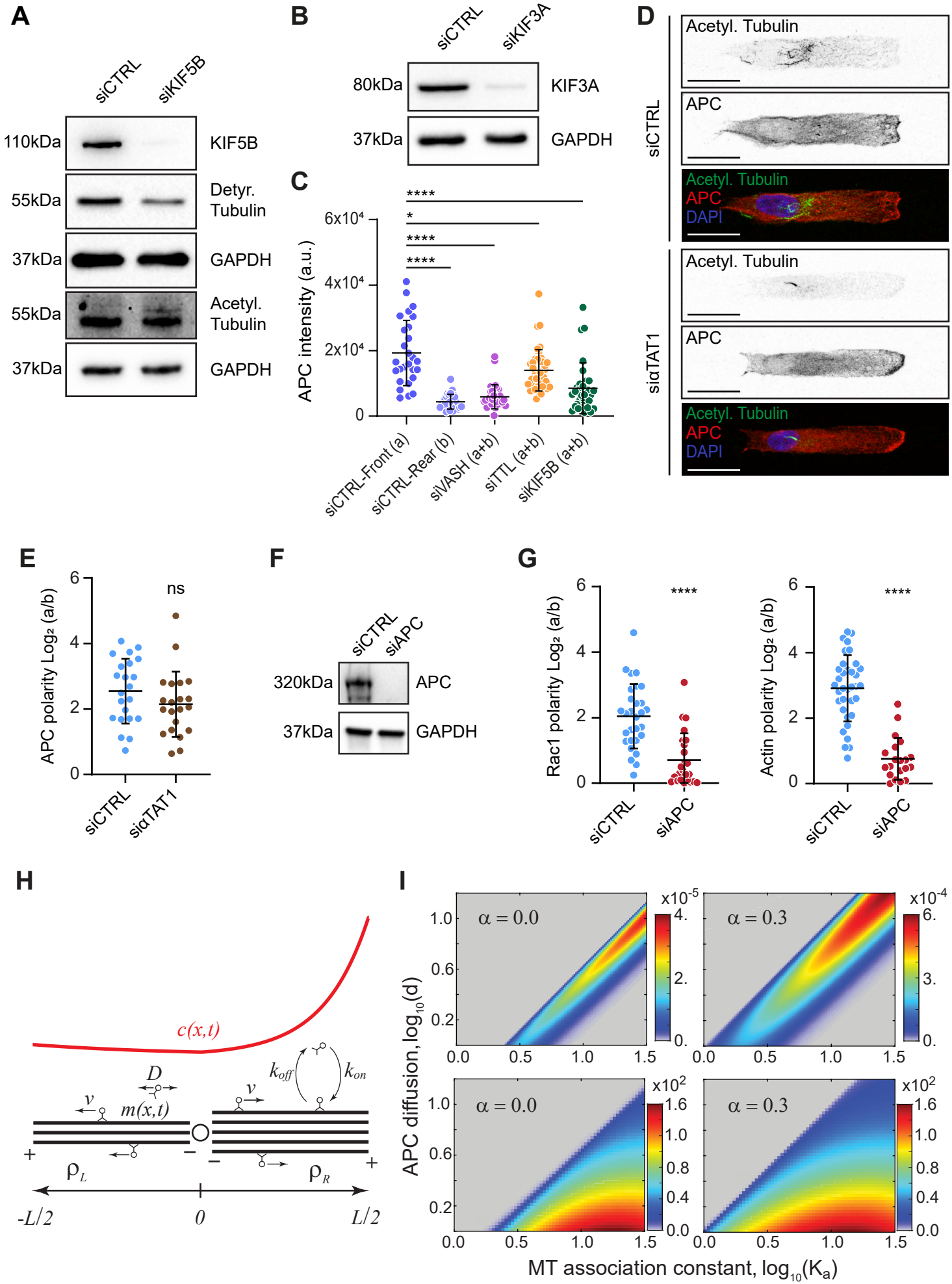
A
siCTRL
siKIF5B
110kDa
KIF5B
55kDa
Detyr. Tubulin
37kDa
GAPDH
55kDa
Acetyl. Tubulin
37kDa
GAPDH
B
siCTRL
siKIF3A
80kDa
KIF3A
37kDa
GAPDH
C
APC intensity (a.u.)
6x10⁴
4x10⁴
2x10⁴
0
****
*
****
****
siCTRL-Front (a)
siCTRL-Rear (b)
siVASH (a+b)
siTTL (a+b)
siKIF5B (a+b)
D
siCTRL
siαTAT1
Acetyl. Tubulin
APC
Acetyl. Tubulin
APC
DAPI
Acetyl. Tubulin
APC
Acetyl. Tubulin
APC
DAPI
E
APC polarity Log₂ (a/b)
ns
siCTRL
siαTAT1
F
siCTRL
siAPC
320kDa
APC
37kDa
GAPDH
G
Rac1 polarity Log₂ (a/b)
****
siCTRL
siAPC
Actin polarity Log₂ (a/b)
****
siCTRL
siAPC
H
c(x,t)
D
v
m(x,t)
v
koff
kon
ρL
ρR
-L/2
0
L/2
I
α = 0.0
α = 0.3
α = 0.0
α = 0.3
APC diffusion, log10(d)
MT association constant, log10(Ka)

Fig. S4. Microtubule detyrosination regulates kinesin-1-based intracellular transport of APC to initiate symmetry-breaking required for directed cell migration

(A) Immunoblot analysis RPE-1 cell lysates treated with control or KIF5B specific siRNAs with antibodies against indicated proteins. GAPDH was used as the loading control.

(B) Immunoblot analysis RPE-1 cell lysates treated with control or KIF3A specific siRNAs with antibodies against respective proteins validating siRNA mediated knockdown. GAPDH was used as the loading control.

(C) Mean APC intensities in RPE-1 cells treated with indicated siRNAs. Data represents the sum of intensities from 10% of normalized area of the edges of the two sides (a + b). (N, n): siCTRL (28,3), siVASH (33,3), siTTL (42,3), siKIF5B (31,3).

(D) Representative point-scanning confocal maximum-intensity projected images of control and αTAT1 depleted RPE-1 cells on linear micropatterns immunostained with antibodies against acetylated α-tubulin and APC with DAPI as a DNA counterstain. Scale bar, 20 μm.

(E) Quantification of APC intensity polarity at the cell edges (a/b) upon siRNA mediated depletion of αTAT1 from immunostained RPE-1 cells. (N, n): siCTRL (22,2), si αTAT1 (21,2).

(F) Representative immunoblot showing depletion of APC achieved using target specific siRNAs.

(G) Quantification of Rac1 and actin intensity polarity at the cell edges (a/b) upon siRNA mediated depletion of APC from immunostained RPE-1 cells. (N, n): Rac1 - siCTRL (29,3), siAPC (24,3), Actin - siCTRL (35,4), siAPC (20,3).

(H) Schematic diagram of the 1D model cell with left and right MT bundles emanating from the centrosome. All notations are as in Methods.

(I) The maximal eigenvalue $\lambda_{max} > 0$ of the unstable symmetric state S of the model, which is approximately inverse of τ_{pol}, (top row) and the cell asymmetry magnitude σ (bottom row) shown as a surface over a log-scaled domain of normalized APC diffusion coefficient d and APC MT association constant K_a. See Methods for details.

N - number of cells, n - number of independent experiments. The scatter plots include mean ± SD. ns - not significant, *$P \leq 0.05$, ****$P \leq 0.0001$.

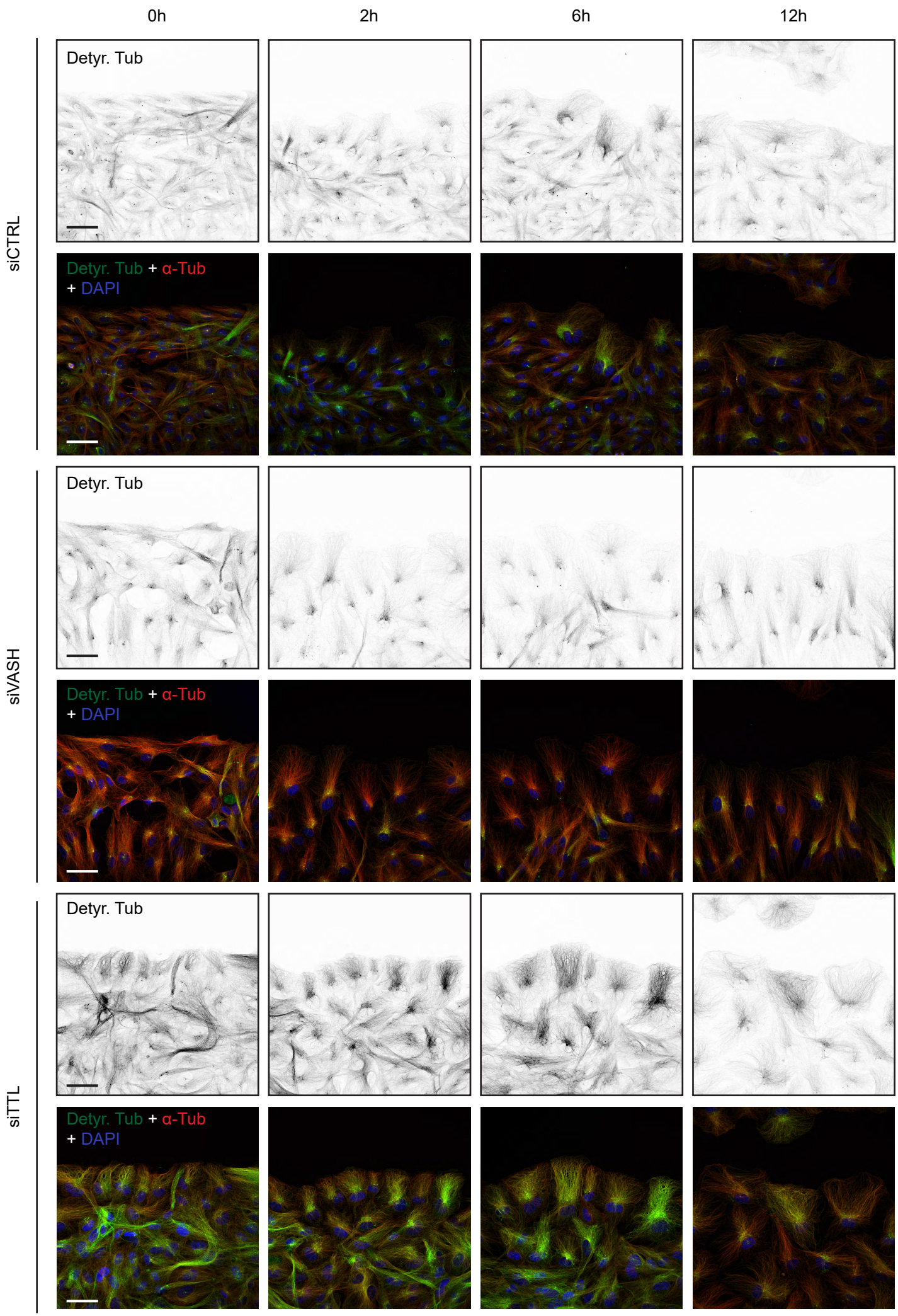
0h
2h
6h
12h
siCTRL
siVASH
siTTL
Detyr. Tub
Detyr. Tub + α-Tub
+ DAPI

Fig. S5. Microtubule detyrosination during 2D-cell migration

Representative point-scanning confocal maximum-intensity projected images of RPE-1 cells treated with indicated siRNAs at indicated time points migrating to close the gap following insert removal. Cells were immunostained with antibodies against detyrosinated (Detyr. Tub) and total α-tubulin with DAPI as nuclear stain. Scale bar, 50 μm.

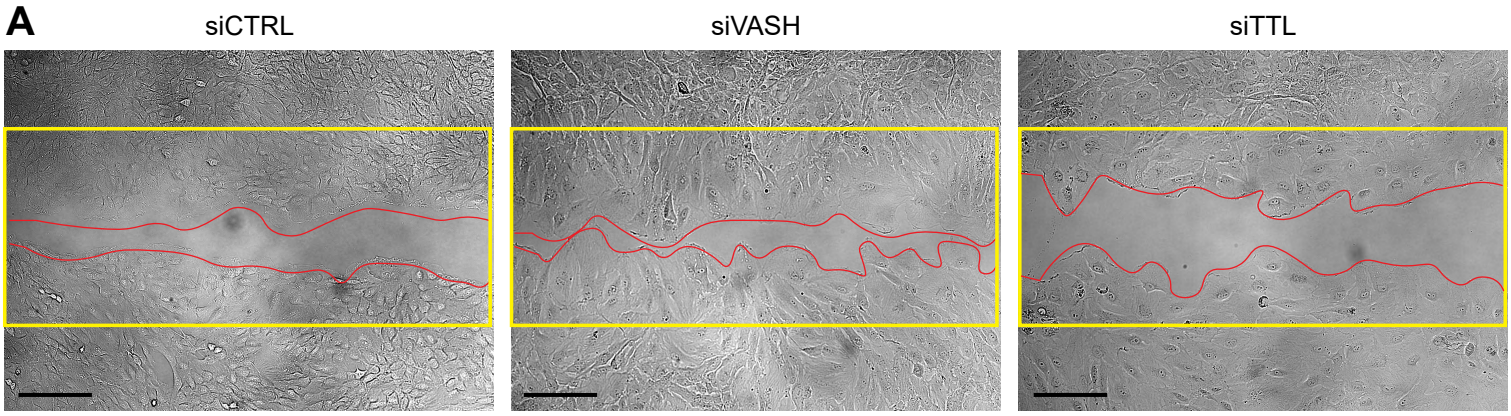
A
siCTRL
siVASH
siTTL

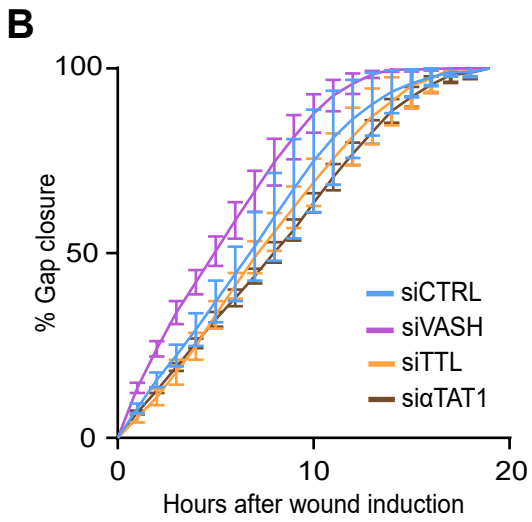
B
100
50
0
% Gap closure
0
10
20
Hours after wound induction
siCTRL
siVASH
siTTL
siαTAT1

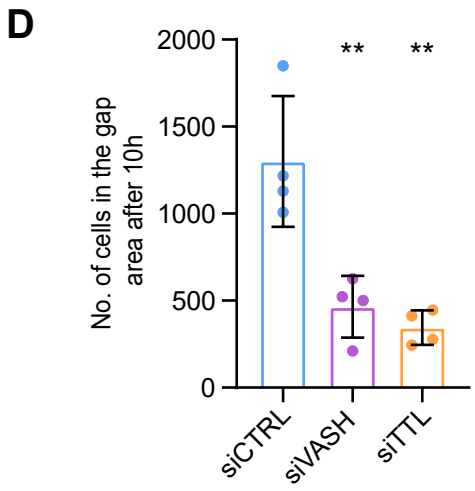
D
2000
1500
1000
500
0
No. of cells in the gap area after 10h
**
**
siCTRL
siVASH
siTTL

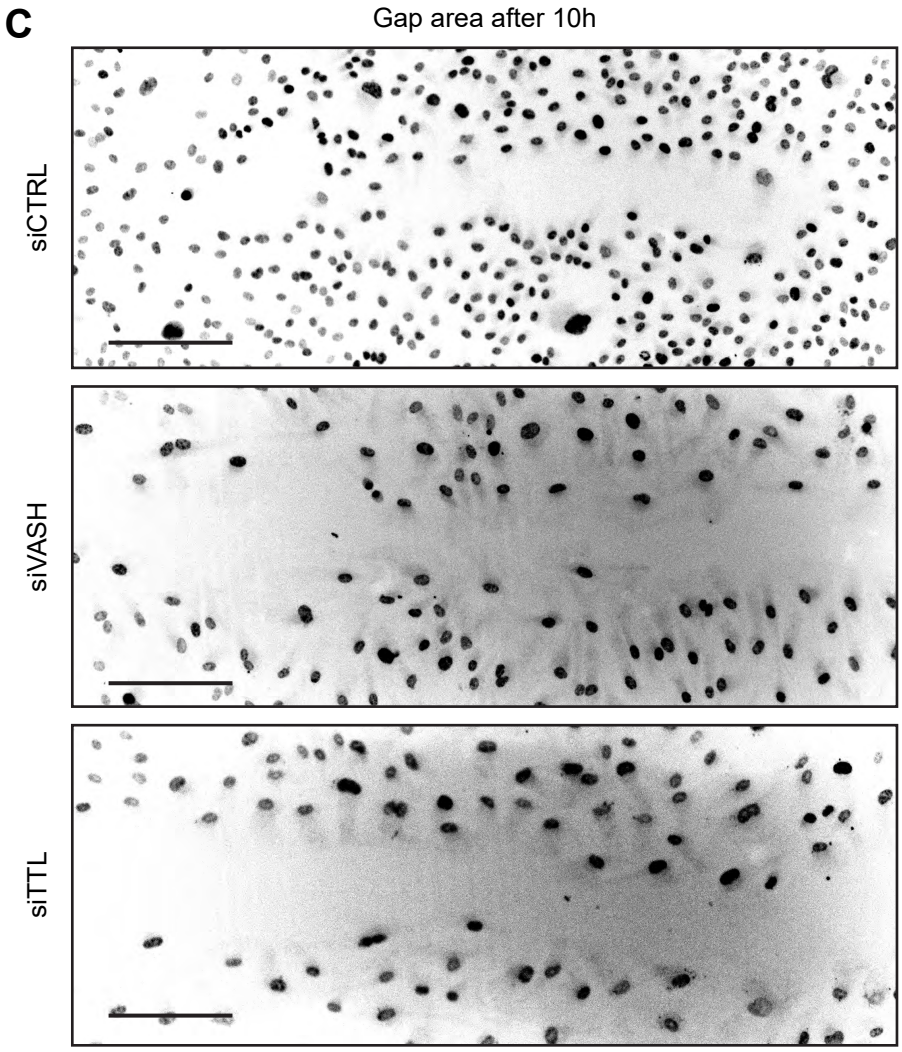
C
Gap area after 10h
siCTRL
siVASH
siTTL

Fig. S6. Microtubule detyrosination is crucial for accurate 2D-cell migration

(A) Representative phase-contrast images of RPE-1 cell migration during gap-closing transfected with indicated siRNAs. Yellow lines indicate the wound edge immediately after insert removal and red lines mark the cell edge after 10 h. Scale bar, 200 μm.

(B) Quantification of percentage of gap-closure over time by RPE-1 cells treated with indicated siRNAs. The line represents the mean and error bar represent SD. N (number of independent experiments): siCTRL (4), siVASH (4), siTTL (4), siαTAT1 (3).

(C) Representative images of RPE-1 cells in the gap area stably expressing H2B-GFP closing the gap with indicated siRNA treatments 10h after insert removal. Scale bar, 200 μm.

(D) Quantification of number of RPE-1 H2B-GFP cells in the gap area 10h after insert removal under indicated treatments. The bar graph shows individual replicate values from four independent experiments, their mean and error bar represent SD.
$^{**}P \leq 0.01$.

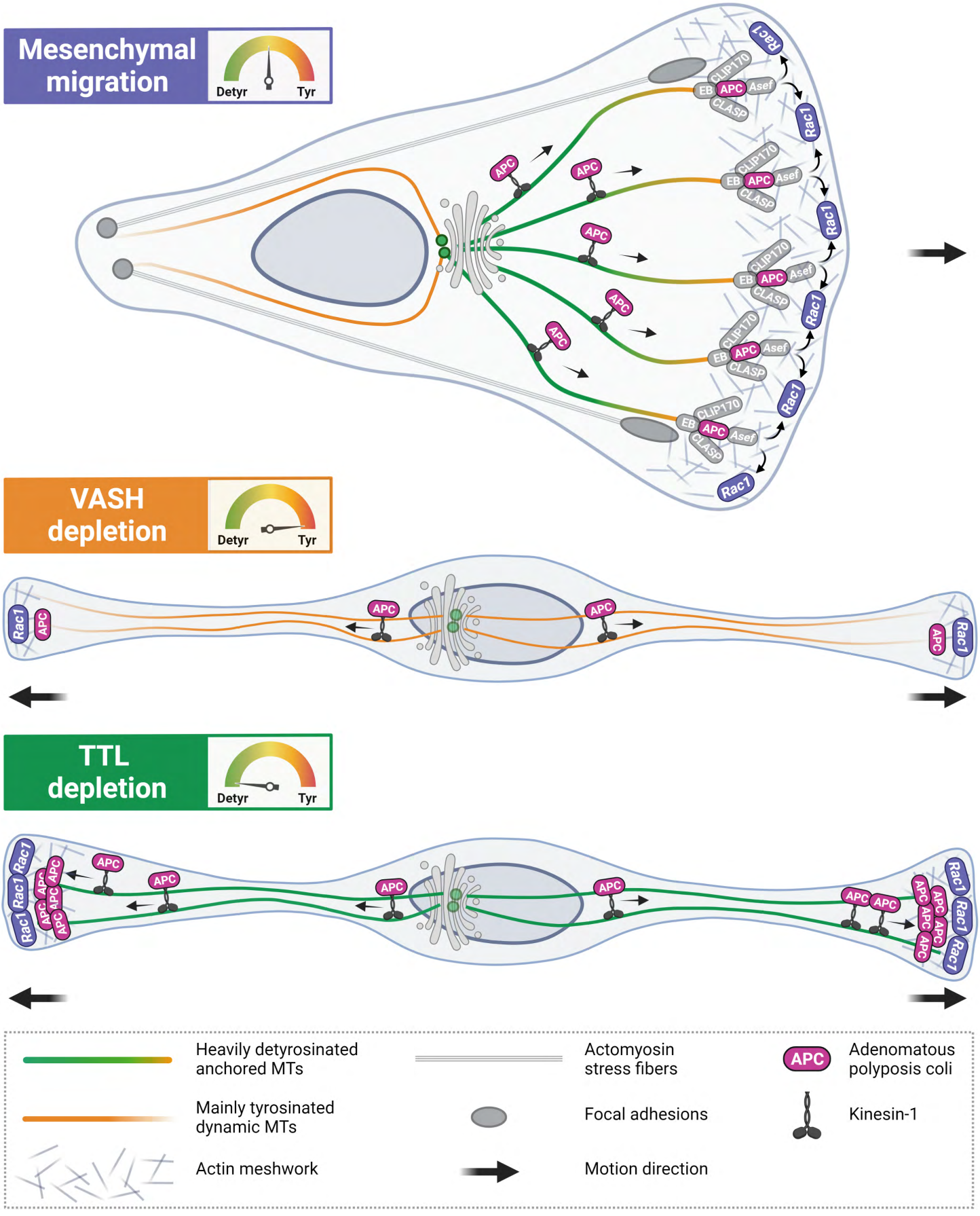
Mesenchymal migration
Detyr
Tyr
Rac1
CLIP170
EB
APC
Asef
CLASP
VASH depletion
TTL depletion
Heavily detyrosinated anchored MTs
Mainly tyrosinated dynamic MTs
Actin meshwork
Actomyosin stress fibers
Focal adhesions
Motion direction
Adenomatous polyposis coli
Kinesin-1

Fig. S7. Microtubule detyrosination is crucial for cell migration in 3D matrices

The model depicts how MT detyrosination stimulates kinesin-1-based transport of APC to the cortical sites, where APC facilitates MT-anchoring and stabilization, as well as Rac1-dependent actin nucleation. APC-accumulation-mediated MT-anchoring leads to higher detyrosination of long-lived MTs and consequently to directed and enhanced kinesin-1-dependent transport of APC, ultimately forming a positive feedback loop between MT detyrosination, stability and APC. Cells with disbalanced detyrosination levels become effectively bipolarized, displaying elongation instead of the directional motion. Created with BioRender.com.

Table S1. Model parameters

Parameter	Value*	References
v, APC-kinesin complex motor velocity	$0.4\ \mu m/sec$	(25-29)
D, APC-kinesin complex cytoplasmic diffusion coefficient	$2.0; 1.0 - 16.0\ \mu m^2/sec$	this study
k_{on}, k_{on}^0, APC-kinesin complex microtubule binding rate	$3.0; 1.0 - 32.0 sec^{-1}$	(29, 30)
k_{off}, APC-kinesin complex microtubule dissociation rate	$1.0\ sec^{-1}$	(29, 31)
L, cell length	$100\ \mu m$	this study

* Parameter values are given as a reference value used for the calculation of data in Figures 6D,F and as the range used for the calculation of data in Figures 6H and S4I.

SI references

1. B. Orr *et al.*, An anaphase surveillance mechanism prevents micronuclei formation from frequent chromosome segregation errors. *Cell reports* **37**, 109783 (2021).
2. K. Hennig *et al.*, Stick-slip dynamics of cell adhesion triggers spontaneous symmetry breaking and directional migration of mesenchymal cells on one-dimensional lines. *Sci Adv* **6**, eaau5670 (2020).
3. S. Vinopal *et al.*, gamma-Tubulin 2 nucleates microtubules and is downregulated in mouse early embryogenesis. *PLoS One* **7**, e29919 (2012).
4. M. Barisic *et al.*, Mitosis. Microtubule detyrosination guides chromosomes during mitosis. *Science* **348**, 799-803 (2015).
5. S. Liao *et al.*, Molecular basis of vasohibins-mediated detyrosination and its impact on spindle function and mitosis. *Cell Res* **29**, 533-547 (2019).
6. T. Shida, J. G. Cueva, Z. Xu, M. B. Goodman, M. V. Nachury, The major alpha-tubulin K40 acetyltransferase alphaTAT1 promotes rapid ciliogenesis and efficient mechanosensation. *Proc Natl Acad Sci U S A* **107**, 21517-21522 (2010).
7. L. Cassimeris, J. Morabito, TOGp, the human homolog of XMAP215/Dis1, is required for centrosome integrity, spindle pole organization, and bipolar spindle assembly. *Mol Biol Cell* **15**, 1580-1590 (2004).
8. V. Gupta, K. J. Palmer, P. Spence, A. Hudson, D. J. Stephens, Kinesin-1 (uKHC/KIF5B) is required for bidirectional motility of ER exit sites and efficient ER-to-Golgi transport. *Traffic* **9**, 1850-1866 (2008).
9. N. Mohan, E. M. Sorokina, I. V. Verdeny, A. S. Alvarez, M. Lakadamyali, Detyrosinated microtubules spatially constrain lysosomes facilitating lysosome-autophagosome fusion. *J Cell Biol* **218**, 632-643 (2019).
10. M. V. Hadjihannas *et al.*, Aberrant Wnt/beta-catenin signaling can induce chromosomal instability in colon cancer. *Proc Natl Acad Sci U S A* **103**, 10747-10752 (2006).
11. T. Matanis *et al.*, Bicaudal-D regulates COPI-independent Golgi-ER transport by recruiting the dynein-dynactin motor complex. *Nat Cell Biol* **4**, 986-992 (2002).
12. Y. Steblyanko *et al.*, Microtubule poleward flux in human cells is driven by the coordinated action of four kinesins. *EMBO J* **39**, e105432 (2020).
13. J. G. DeLuca, Kinetochore-microtubule dynamics and attachment stability. *Methods Cell Biol* **97**, 53-79 (2010).
14. I. S. Nathke, C. L. Adams, P. Polakis, J. H. Sellin, W. J. Nelson, The adenomatous polyposis coli tumor suppressor protein localizes to plasma membrane sites involved in active cell migration. *J Cell Biol* **134**, 165-179 (1996).
15. L. M. Meenderink *et al.*, P130Cas Src-binding and substrate domains have distinct roles in sustaining focal adhesion disassembly and promoting cell migration. *PLoS One* **5**, e13412 (2010).
16. G. Rajendraprasad, S. Eibes, C. G. Boldu, M. Barisic, TH588 and Low-Dose Nocodazole Impair Chromosome Congression by Suppressing Microtubule Turnover within the Mitotic Spindle. *Cancers (Basel)* **13** (2021).
17. R. Gorelik, A. Gautreau, Quantitative and unbiased analysis of directional persistence in cell migration. *Nat Protoc* **9**, 1931-1943 (2014).
18. L. Laan, J. Husson, E. L. Munteanu, J. W. Kerssemakers, M. Dogterom, Force-generation and dynamic instability of microtubule bundles. *Proc Natl Acad Sci U S A* **105**, 8920-8925 (2008).

19. N. Pavin, L. Laan, R. Ma, M. Dogterom, F. Jülicher, Positioning of microtubule organizing centers by cortical pushing and pulling forces. *New J Phys* **14**, 105025 (2012).
20. C. Leduc *et al.*, Molecular crowding creates traffic jams of kinesin motors on microtubules. *Proc Natl Acad Sci U S A* **109**, 6100-6105 (2012).
21. D. Seetapun, D. J. Odde, Cell-length-dependent microtubule accumulation during polarization. *Curr Biol* **20**, 979-988 (2010).
22. A. J. Zwetsloot, G. Tut, A. Straube, Measuring microtubule dynamics. *Essays Biochem* **62**, 725-735 (2018).
23. T. McHugh, J. P. I. Welburn, Potent microtubule-depolymerizing activity of a mitotic Kif18b-MCAK-EB network. *J Cell Sci* **136** (2023).
24. M. Zhen, *Numerical bifurcation analysis for reaction-diffusion equations*, Springer series in computational mathematics (Springer Verlag, Berlin Heidelberg, 2000), pp. XIV, 414.
25. D. Cai, K. J. Verhey, E. Meyhöfer, Tracking single Kinesin molecules in the cytoplasm of mammalian cells. *Biophys J* **92**, 4137-4144 (2007).
26. N. Kaul, V. Soppina, K. J. Verhey, Effects of α-tubulin K40 acetylation and detyrosination on kinesin-1 motility in a purified system. *Biophys J* **106**, 2636-2643 (2014).
27. J. Xu, Z. Shu, S. J. King, S. P. Gross, Tuning multiple motor travel via single motor velocity. *Traffic* **13**, 1198-1205 (2012).
28. M. Sirajuddin, L. M. Rice, R. D. Vale, Regulation of microtubule motors by tubulin isotypes and post-translational modifications. *Nat Cell Biol* **16**, 335-344 (2014).
29. G. Arpağ *et al.*, Motor Dynamics Underlying Cargo Transport by Pairs of Kinesin-1 and Kinesin-3 Motors. *Biophys J* **116**, 1115-1126 (2019).
30. C. Leduc *et al.*, Cooperative extraction of membrane nanotubes by molecular motors. *Proc Natl Acad Sci U S A* **101**, 17096-17101 (2004).
31. J. P. Bergman *et al.*, Cargo navigation across 3D microtubule intersections. *Proc Natl Acad Sci U S A* **115**, 537-542 (2018).

Movie Legends

Movie S1 (separate file). Microtubule detyrosination is essential for cell polarity and directed cell migration

Live-cell imaging of RPE1 cell migration on linear micropatterns following treatments with control and target specific siRNAs. Uniform time stamp for all treatments. Time, hours:min.

Movie S2 (separate file). Microtubule detyrosination regulates focal adhesion dynamics

Spinning-disk confocal time-series of focal adhesion dynamics from RPE1 cells stably expressing GFP-Vinculin on linear micropatterns, treated with indicated siRNAs.

Movie S3 (separate file). Microtubule detyrosination is essential for cell polarity and directed cell migration

Live-cell imaging of U2OS cell migration on linear micropatterns following treatments with control and target specific siRNAs. Uniform time stamp for all treatments. Time, hours:min.

Movie S4 (separate file). Microtubule detyrosination regulates microtubule dynamics during directed cell migration

Spinning-disk confocal time-series of EB1 dynamics from U2OS cells stably expressing EB1-GFP on linear micropatterns, treated with indicated siRNAs. Uniform time stamp for all treatments. Time, min:sec.

Movie S5 (separate file). Microtubule detyrosination regulates microtubule dynamics during directed cell migration

Live-cell imaging of RPE1 cell migration on linear micropatterns following indicated treatments. Uniform time stamp for all treatments. Time, hours:min.

Movie S6 (separate file). Microtubule detyrosination regulates kinesin-1-based intracellular transport of APC to initiate symmetry-breaking required for directed cell migration

Live-cell imaging of RPE1 cell migration on linear micropatterns following treatment with indicated siRNAs. Uniform time stamp for all treatments. Time, hours:min.

Movie S7 (separate file). Microtubule detyrosination regulates kinesin-1-based intracellular transport

Spinning-disk confocal time-series of GFP-Rab6 transport in RPE1 cells on linear micropatterns, treated with indicated siRNAs. Uniform time stamp for all treatments. Time, min:sec.

Movie S8 (separate file). Microtubule detyrosination is crucial for cell migration in 3D matrices

Phase-contrast live-cell imaging of RPE1 cell migration in 3D-matrix following treatment with indicated siRNAs. Uniform time stamp for all treatments. Time, hours:min.